Supporting Information

Li-In alloy anode and Nb_2CT_X artificial solid-electrolyte interphase for practical Li metal batteries.

Seunghun Lee[†, a, b], Mun Sek Kim [†c], Jung-Hoon Lee [d], Ji-Hyun Ryu[a, b], Vandung Do [a], Byeong Gwon Lee[a,b], Woong Kim*[b] and Won Il Cho*[a, b]

[a] Center for Energy Storage Research, Korea Institute of Science and Technology (KIST), Hwarangno 14 -gil 5, Seongbuk-gu, Seoul, 02792, Republic of Korea

[b] Department of Materials Science and Engineering, Korea University, 145 Anam-ro, Seongbuk-gu, Seoul, 02841, Republic of Korea

[c] Department of Chemical Engineering, Stanford University, 450 Serra Mall, Stanford, California, 94305, USA.

[d] Computational Science Research Center, Korea Institute of Science and Technology (KIST), Hwarangno 14 -gil 5, Seongbuk-gu Seoul, 02792, Republic of Korea

[†] first author

*Corresponding Author

W. Kim. E-mail: woongkim@korea.ac.kr

W. I. Cho. E-mail: wonic@kist.re.kr

This supporting figure includes:

Fig. S1. Li-In phase diagram[1].

Fig. S2. XRD patterns of Li-In alloy anode after Li stripping or plating

Fig. S3. BSE, EDX element mapping, FIB-SEM cross-sectional image of Li-In alloy anode after Li stripping.

Fig. S4. Molecular structure of $Li_{13}In_3$ unit cell and Li diffusion pathway on (311) surface of $Li_{13}In_3$.

Fig. S5. SEM image and corresponding EDX element mapping image of Nb_2CT_X MXene and Nb_2AlC MAX phase.

Fig. S6. XRD patterns of Nb_2AlC and Nb_2CT_X.

Fig. S7. Wide scan XPS spectra of Nb_2CT_X MXene and Nb_2AlC MAX phase.

Fig. S8. Optical image of manufacturing process and SEM images of Nb_2CT_X Li-In anode.

Fig. S9. XRD profile of $Nb2CT_X$ Li-In anode.

Fig. S10. Practical areal capacity measurement of Nb_2CT_X Li-In anode.

Fig. S11. SEM surface morphologies of Li anode and Li-In alloy anode after re-electrodeposition of Li.

Fig. S12. Galvanostatic Li stripping/plating voltage profile.

Fig. S13. Full cell cycling performance and corresponding voltage profile of Nb_2CT_X Li anode.

Fig. S14. AC impedance measurement for Li|NCM 811, Li-In|NCM 811, Li-In Nb_2CT_X|NCM 811.

Fig. S15. Li-In foil thickness and further roll-pressing results.

Table S1. The calculation for termination group formation energy and Li binding energy on the Nb_2CT_X surface.

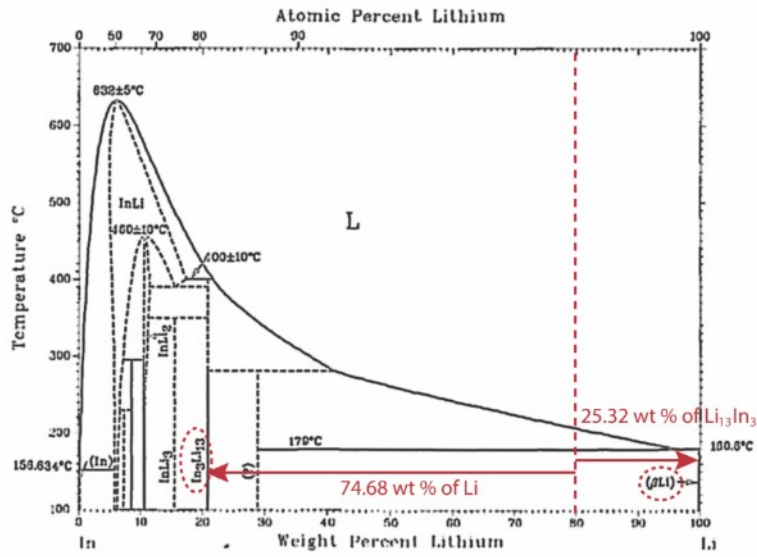Table S2. Li-In foil thickness before and after roll-pressing.

Fig. S1. Li-In phase diagram. The red dashed vertical line represents 80 wt% of Li (98.51 at % of Li) and 20 wt % of In (1.49 at % of In) composition. At the designed composition, Li-In alloy consists of 74.68 wt % of Li and 25.32 wt % of $Li_{13}In_3$.
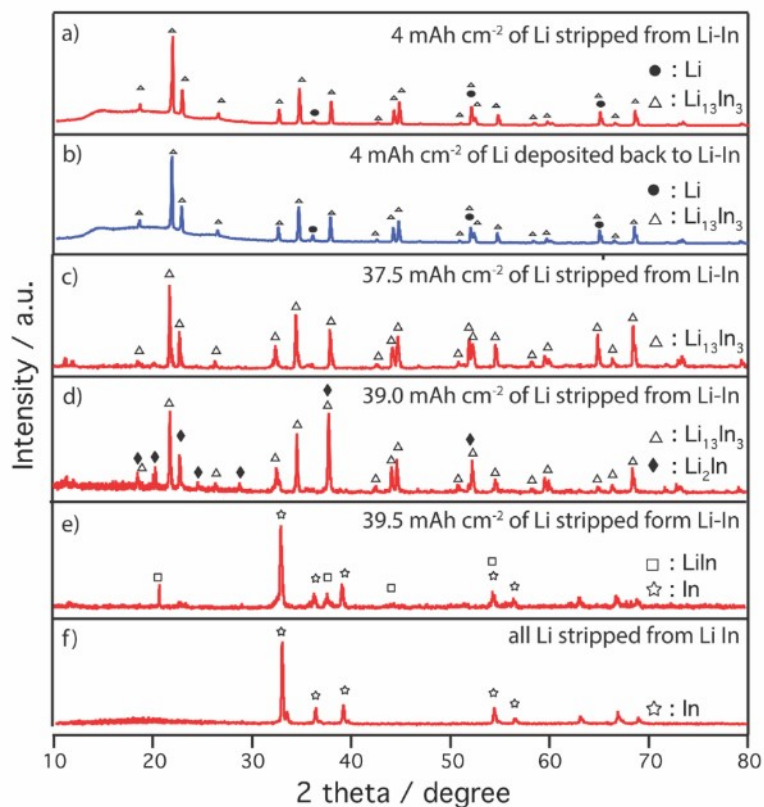
Fig. S2. XRD patterns for Li-In alloy anode after a) 4 mAh cm^{-2} of Li stripped, b) 4 mAh cm-2 Li deposited back to a), c) 37.5 mAh cm^{-2}, d) 39.0 mAh cm^{-2}, e) 39.5 mAh cm^{-2}, f) all of Li stripped from Li-In alloy anode. Phase transition from $Li_{13}In_3$ to In was observed after 37.5 mAh cm^{-2} of Li stripped ($Li_{13}In_3 \rightarrow Li_2In \rightarrow LiIn \rightarrow In$). XRD peak of Li, $Li_{13}In_3$, Li_2In, LiIn, and In notice with the filled circle, empty-triangle, filled-diamond, empty-square, and empty-star shape, respectively.
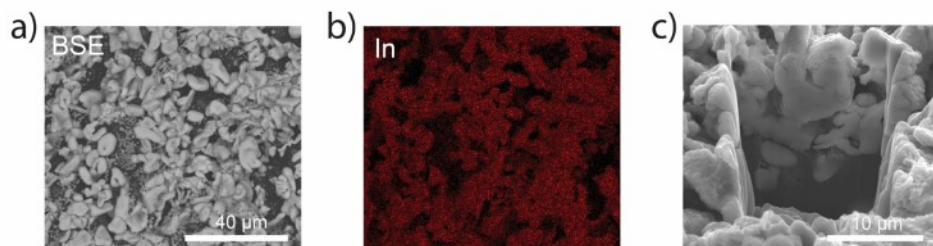
Fig. S3. a) SEM BSE mode micrographs of the Li-In alloy anode after 4 mAh cm^{-2} galvanostatic stripping of Li using Li-In|Li-In symmetric cell. Bright particles are Li-In alloy (Li$_{13}$In$_3$), and the dark background is pristine Li. b) Corresponding EDX element mapping image for In (red). c) FIB cross-section image of Li-In after Li stripping with the same conditions as a). In the electrode's upper region, most of the Li was stripped, and only the light-colored Li1$_3$In$_3$ remains, showing an irregular porous structure, and the remained Li shows dark in the lower part of the image.
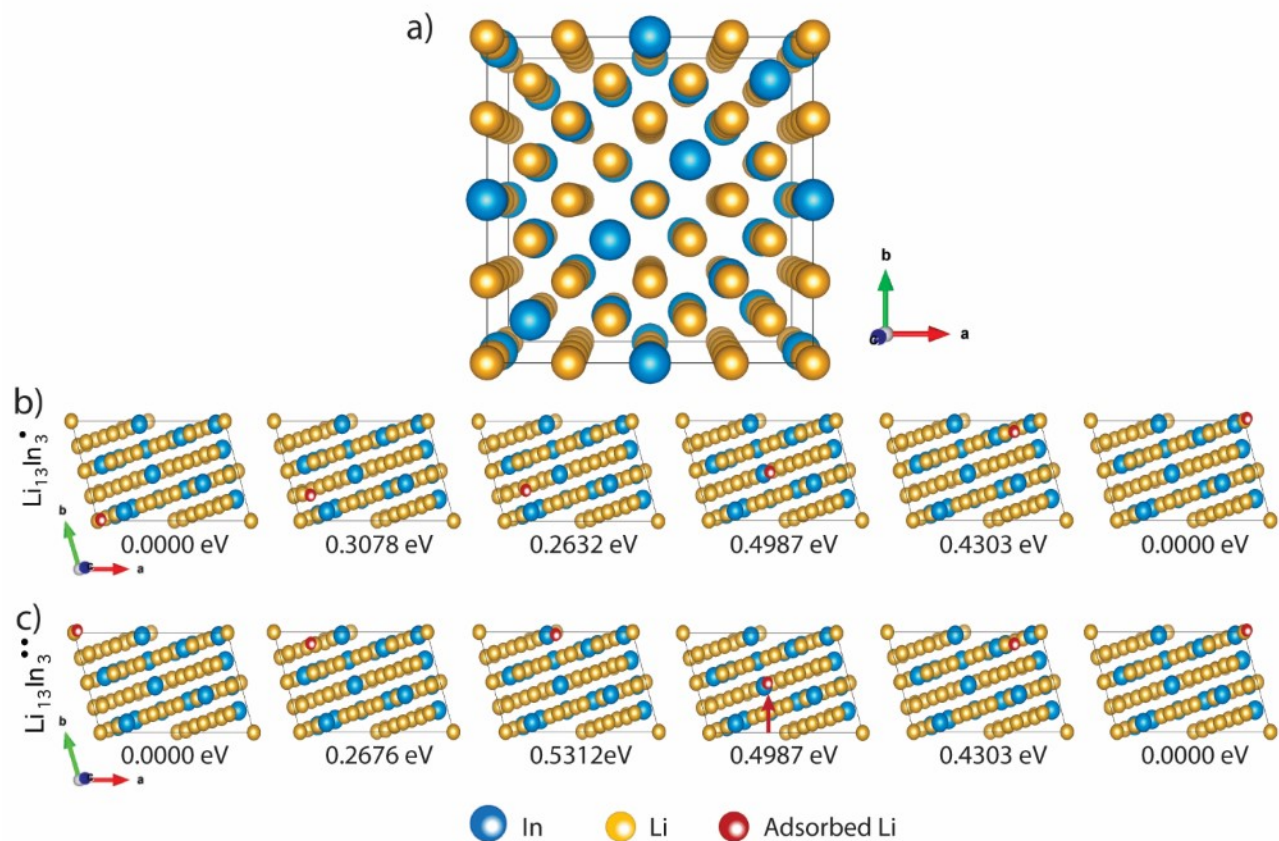
Fig. S4. a) The optimized crystal structure of $Li_{13}In_3$. The space group is the cubic $Fd\overline{3}m$ with the lattice parameters a = b = c = 13.55 Å and $\alpha = \beta = \gamma = 90°$. Visualization of the Li migration on the (311) surface of the $Li_{13}In_3$ along b) pathway 1 ($Li_{13}In_3{}^{\bullet}$), c) pathway 2 ($Li_{13}In_3{}^{\bullet\bullet}$). The first configuration is the initial state of the diffusion process that Li adsorbed on the most stable adsorption site on the (311) of $L_{13}In_3$ and considered as 0 eV. The adsorbed Li migrates following its stable energetic position, and each image shows the Li when it was located at a local minimum. Values below each image are relative energy calculated with respect to the energy at the initial state. Blue and yellow spheres are In and Li of $L_{13}In_3$, and the red sphere is the migrating Li adatom.

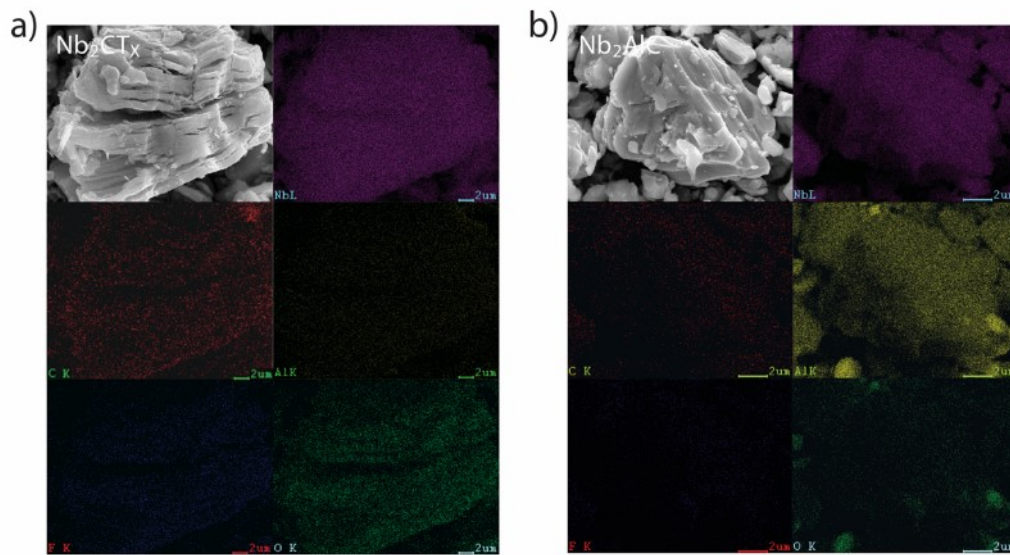Fig. S5. SEM image and EDX element mapping images of a) Nb_2CT_X (MXene) and b) Nb_2AlC (MAX phase). EDX element mapping images in both contents correspond with Nb L (purple), C K (red), Al K (yellow), F K (blue), O K (oxygen) peak.
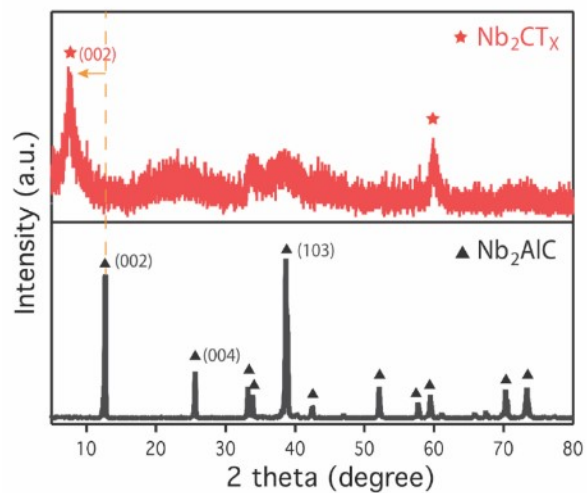
Fig. S6. XRD profiles of Nb$_2$AlC (bottom, black) and Nb$_2$CT$_X$ (top, red). Marks on the graph correspond to the major XRD peaks Nb$_2$AlC (black triangle), Nb$_2$CT$_X$ (red star). After the synthesis, significant changes of several peaks indicate the transformation of MAX phase to MXene; the (103) peak of Nb$_2$AlC, around 2 of 39 , disappears after synthesis, and the (002) peak of Nb$_2$AlC corresponding to 2 of 12.9 shifts to a lower angle. Disappeared (103) peak represents that Al layer was removed, and shifted (002) peak means that inter-layer space of Nb$_2$CT$_X$ was increased.
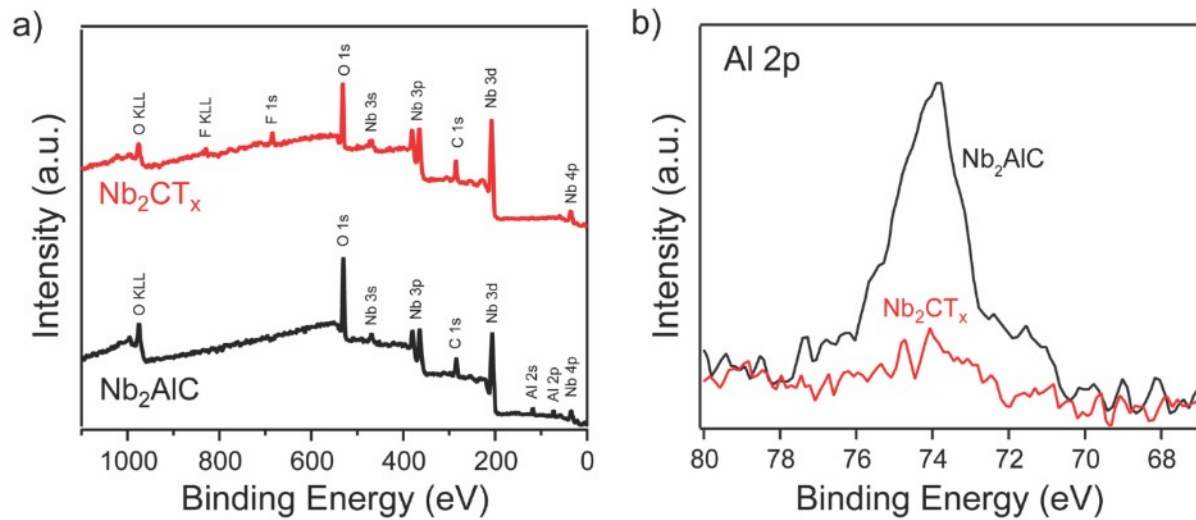
Fig. S7. a) Wide scan XPS spectra of Nb_2CT_X (MXene) and Nb_2AlC (MAX phase), b) High resolution

XPS spectra of Nb_2AlC (black) and Nb_2CT_X (red) at Al 2p region.
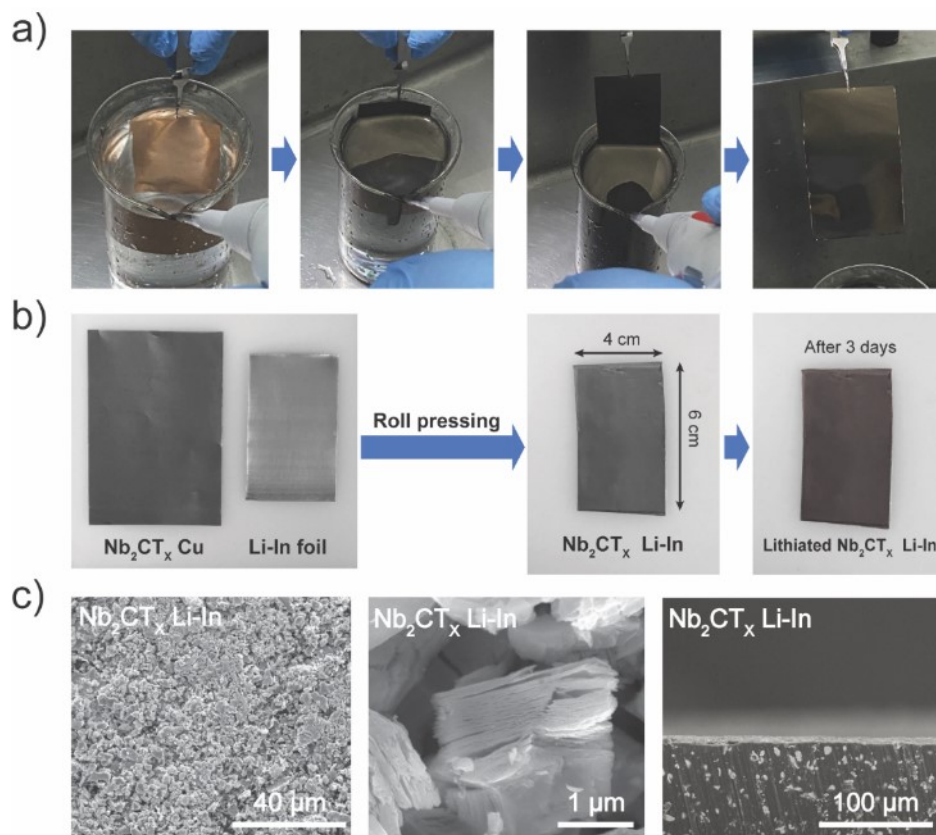
Fig. S8. Preparation and morphologies of the Nb_2CT_X Li-In anodes. Optical image of the a) Nb_2CT_X ASEI on Cu foil using the Langmuir–Blodgett scooping (LBS) method; b) Nb_2CT_X Cu and Li-In foil (left), Nb_2CT_X Li-In right after Nb_2CT_X ASEI transfer to Li-In via roll pressing (middle) and Nb_2CT_X Li-In after 3 days in a dry capsule (right). c) Large-area SEM image (left, top view), enlarged SEM image (middle, top view), and SEM image (right, cross section view) of the Nb_2CT_X Li-In anode.
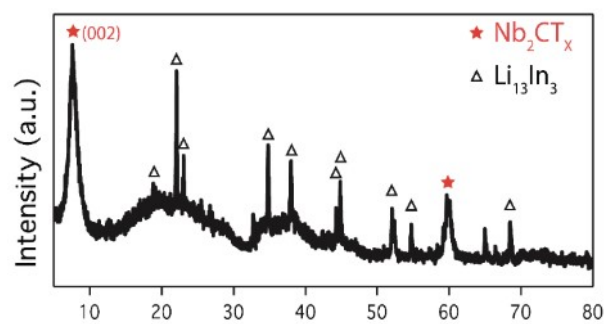
Fig. S9. XRD profile of the Nb_2CT_X Li-In anode. The XRD peaks of Nb_2CT_X and $Li_{13}In_3$ are indicated by the filled star

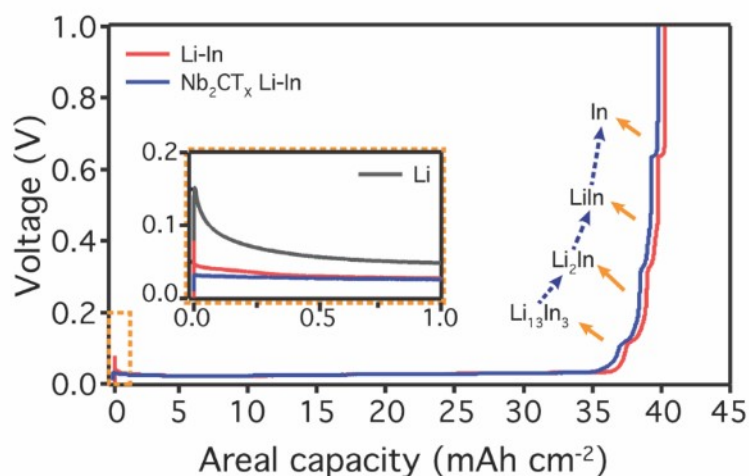and empty triangle symbols, respectively.

Fig. S10. Practical areal capacity measurement for Nb_2CT_X Li-In and Li-In alloy anode using symmetric cell. Voltage profile taking at a fixed current density of 1 mA cm^{-2} with voltage cut-off at 1V. The areal masses of Nb_2CT_X Li-In and Li-In alloy anodes are 13.52 mg cm^{-2} and 13.24 mg cm^{-2}. Capacities of Nb_2CT_X Li-In and Li-In alloy anodes are 39.63 mAh cm^{-2} (2926.64 mAh g^{-1}) and 39.97 mAh cm^{-2} (3021.44 mAh g^{-1}). The areal capacity of Nb_2CT_X Li-In alloy anode was slightly reduced due to pressure during roll pressing process for transfer of Nb_2CT_X ASEI. The inset shows the enlarged voltage profile from 0 to 1.0 mAh cm^{-2} with voltage profile of pure Li from Fig. 1b.
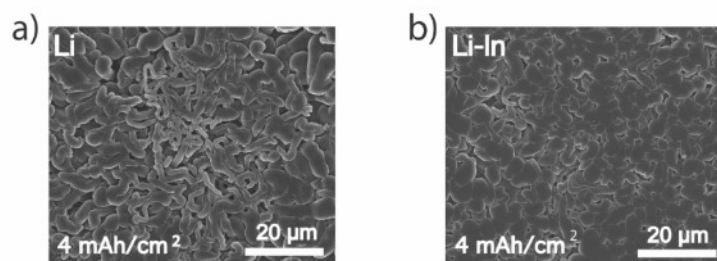
Fig S11. SEM surface morphologies of galvanostatic Li re-electrodeposition onto the f) Li anode and g) Li-In alloy anode after Li stripping of 4mAh cm^{-2} at a fixed current density of 1 mAh cm^{-2} and capacity of 4 mAh cm^{-2}.
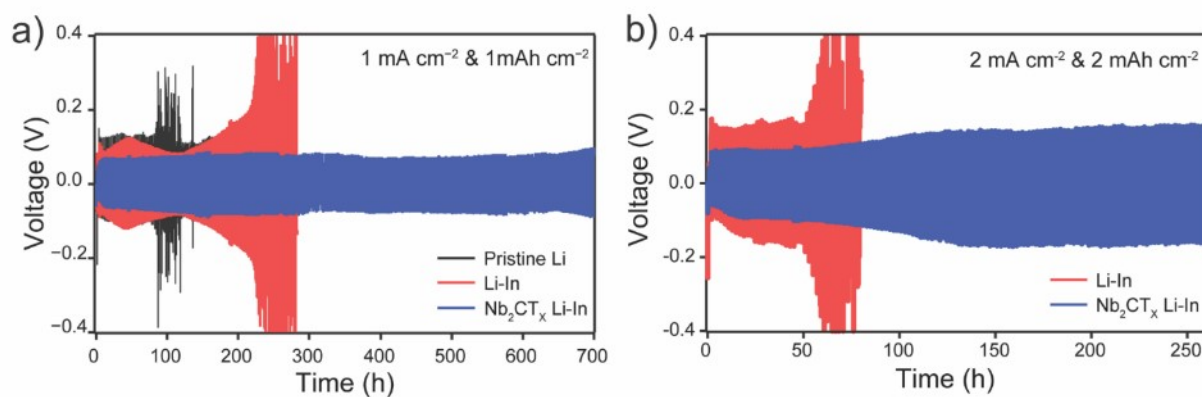

Fig. S12. Galvanostatic Li stripping/plating voltage profiles for the Li (black), Li-In (red) and Nb$_2$CT$_X$ ASEI Li-In (blue) anodes. Voltage profiles were measured by Li|Li, Li-In|Li-In, and Li-In Nb$_2$CT$_X$|Nb$_2$CT$_X$ Li-In symmetric cells at a) 1 mA cm^{-2}/1 mAh cm^{-2} and b) 2 mA cm^{-2}/2 mAh cm^{-2}.
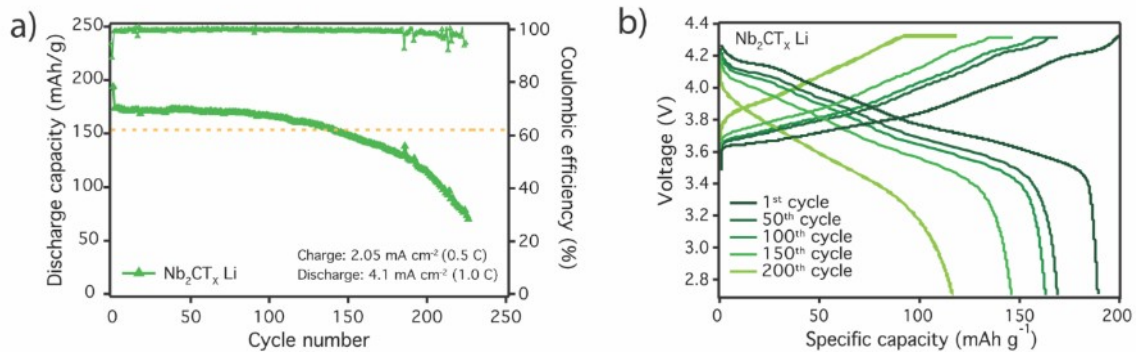
Fig. S13. a) Electrochemical full cell cycling performance with Li Nb$_2$CT$_X$|NCM811 based on discharge capacity (filled symbols, left axis) and Coulombic efficiency (empty symbols, right axis). The full cell was fabricated at an n/p ratio of 11.0 and by using an electrolyte of 8.6 µL mAh^{-1}. Operating conditions of full-cell cycling were 0.5 C for charging, 1.0 C for discharging, and voltage window of 2.7–4.3 V. The first highest discharge capacity point was measured at formation cycle (0.1 C charge & discharge); the yellow dashed line indicates 80% of the initial discharge capacity of each cell. b) Corresponding voltage profiles of Li Nb$_2$CT$_X$|NCM811.
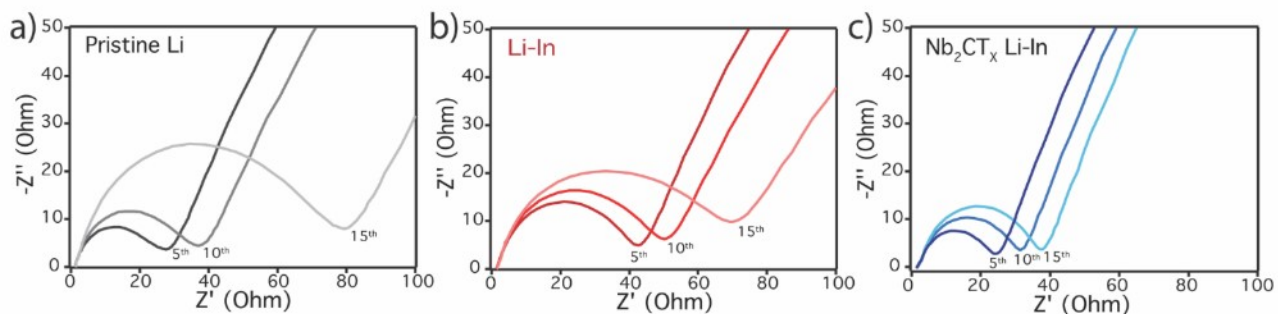
Fig. S14. Nyquist plots after 1st, 5th, 10th, and 15th cycle for a) Li|NCM811, b) Li-In|NCM811, c) Li-In Nb₂CT$_X$|NCM811 full cell.
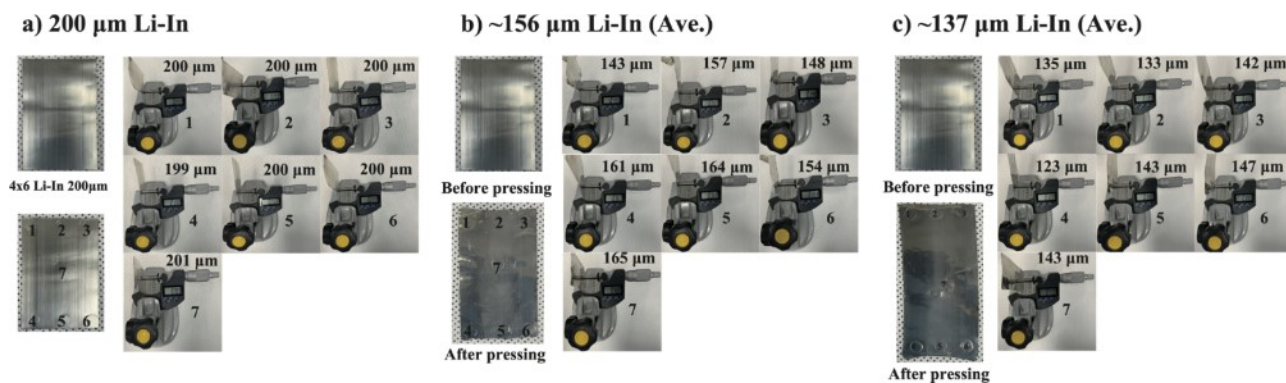

Fig. S15. Li-In foil thickness and roll-pressing results.   a) Pristine Li-In foil from the company (Honzo metal, Japan), b) roll-pressed Li-In foil (average thickness of ~156 μm), and c) roll-pressed Li-In foil (average thickness of ~137 μm).
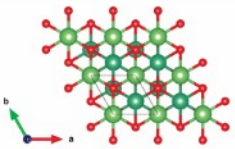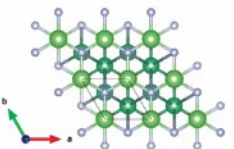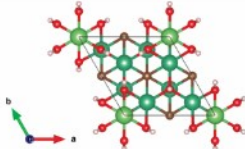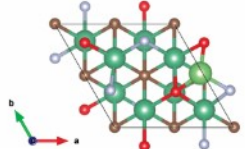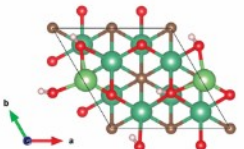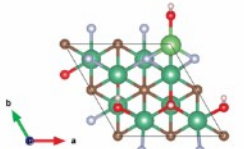
	Nb$_2$C-O-Li	Nb$_2$C-F-Li	Nb$_2$C-OH-Li
Atomic structure			
Termination group formation E	-7.213 eV	-6.238 eV	-6.209 eV
Li binding E	-1.577 eV	-1.516 eV	+0.814 eV
	Nb$_2$C-O, F-Li	Nb$_2$C-O, OH-Li	Nb$_2$C-F, OH-Li
Atomic structure			
Termination group formation E	-6.663 eV	-6.846 eV	-6.279. eV
Li binding E	-1.409 eV	-0.818 eV	-0.249. eV

● Nb ● C ● Li ● F ● O ● H

Table S1. The calculation of termination group formation energy and Li binding energy on the Nb$_2$C (MXene) surface. Images in the table are Nb$_2$CT$_X$ atomic structure with termination groups and Li adatoms. Cyan blue, brown, green, purple, red, and pink spheres are Niobium, Carbon, Lithium, Fluorine, Oxygen, and Hydrogen atom, respectively.

No.	Thickness (μm)								
	1	2	3	4	5	6	7	Ave.	Max. error
a)	200	200	200	199	200	200	201	200	1
b)	143	157	148	161	164	154	165	156	13
c)	135	133	142	123	143	137	143	137	12

Table S2. Li-In foil thickness before and after roll-pressing from Fig. S15

References

1   J. Sangster and A. D. Pelton, 1991, **12**, 290–292.